ADVANCED PHOTONICS RESEARCH Open Access
www.adpr-journal.com

Miniaturized Vertical-Cavity Surface-Emitting Laser Array with a Novel Electrode Design for High-Speed, Low-Noise, and High-Brightness Performance

*Zuhaib Khan, Min-Long Wu, Cheng-Wei Lin, Cheng-Chun Chen, Chia-Jui Chang, Tien-Chang Lu, Nikolay Ledentsov Jr., Nikolay Ledentsov, and Jin-Wei Shi**

Herein, it is shown how the novel layout and arrangement of electrodes of a vertical-cavity surface-emitting laser (VCSEL) array can simultaneously improve its high-speed data transmission performance and the brightness of the output beam. In contrast to the layout of the traditional VCSEL array with its isolated mesas and a single electrode to electrical parallel arrangement of all active elements, the new inverse design can effectively reduce the pitch size between neighboring light emission apertures thereby allowing significant downscaling of the whole active area of the array and high brightness output. Moreover, there are two separate electrodes in demonstrated compact 7 $\times$ 7 VCSEL array, one for pure dc current injection and the other for large ac signal modulation. Compared with the single electrode reference device, the demonstrated array shows heavier dampening of the electrical–optical (E–O) frequency response, a wider maximum 3-dB E–O bandwidth (17 vs 13 GHz), and a Gaussian-like optical far-field pattern with a higher brightness output (65.95 vs 40.8 kW cm^{-2} sr^{-1}), under the same high output power ($\approx$145 mW). The advantages of this novel VCSEL array lead to a much better quality of 32 Gbps eye-opening with a higher brightness output.

1. Introduction

The market for high-brightness (HB) semiconductor laser (SL) sources for various applications such as advanced time-of-flight (ToF) LiDAR,[1,2] motion or vibration monitoring,[3] optical wireless communication,[4–6] and laser manufacturing,[7] is booming. The recent demand for optical wireless communication (OWC) channels for next-generation 5G, 6G, and satellite communication has driven the development of HB light sources for high-speed modulation which can effectively reduce the serious diffraction loss in OWC between satellites[4,5] where wireless linking distances of up to hundreds of kilometers are necessary.[5]

To increase the brightness of the laser output, it is necessary to downscale the active light emission area, narrow the far-field divergence angle, and increase the output power.[8] Although a photonic crystal (PC)-based surface-emitting laser with a state-of-the-art brightness of output optical beam has been demonstrated,[8] no report of its high-speed modulation performance has yet been made. This may be due to the challenge of the extremely long coherence length (time) inside its large optical cavity. The other effective way to realize a high-brightness light source is to build the vertical-cavity surface-emitting laser (VCSEL) array from several single mode (SM) VCSEL units[9,10] which normally exhibit a narrow divergence angle and perfect Gaussian beam output. A moderate to large size of current-confined aperture (>7 μm) and lowering of the distributed Bragg reflector (DBR) mirror reflectivity (<99.7%) are both necessary for high SM power. However, the low DBR mirror reflectivity indicates a short photon lifetime inside the VCSEL cavity and results in a more noticeable resonance in the relative intensity noise (RIN) spectrum.[6,11,12] In addition, the photon density at the center of the large light emission aperture of a VCSEL with high SM output power is usually high, leading to a serious spatial hole burning (SHB) effect and unwanted low-frequency roll-off in the electrical-to-optical (E–O) frequency response.[13,14] These characteristics can cause serious degradation of the high-speed and large-signal transmission of a high-power/high-brightness VCSEL array. One possible way to overcome the aforementioned problems in SM VCSELs and to

Z. Khan, M.-L. Wu, C.-W. Lin, J.-W. Shi
Department of Electrical Engineering
National Central University
Taoyuan 320, Taiwan
E-mail: jwshi@ee.ncu.edu.tw

C.-C. Chen, C.-J. Chang, T.-C. Lu
Department of Photonics and institute of Electro-Optical Engineering
College of Electrical and Computer Engineering
National Yang Ming Chiao Tung University
Hsinchu 30050, Taiwan

N. Ledentsov Jr., N. Ledentsov
Vertically Integrated Systems, GmbH
10623 Berlin, Germany

The ORCID identification number(s) for the author(s) of this article can be found under https://doi.org/10.1002/adpr.202300072.

DOI: 10.1002/adpr.202300072

sustain a high-quality of output beam with high CW power (>200 mW) would be to combine 905 or 940 nm multimode VCSEL units with a backside substrate lens.[15,16] However, the size limitation of each backside lens to be integrated impedes the dense arrangement of VCSEL units and will eventually limit the brightness performance.

In this work, we demonstrate a 7 × 7 coupled cavity 850 nm VCSEL array using a novel design for both the layout of the ultra-compact array and the electrode pads. This design can overcome the SHB problem and relax the trade-offs between the divergence angle of the far-field pattern (FFP), the speed, and the RIN resonance in the SM VCSEL. A high maximum CW quasi-SM optical power (145 mW at 275 mA) with Gaussian FFPs and a narrow divergence angle ((FWHM): 8°) can be simultaneously achieved together with a miniaturization of the light emission active area (120 × 120 μm^2). Moreover, this HB source also exhibits heavy damping and a flat E–O frequency response, a wide 3-dB bandwidth (17 GHz), and clear 32 Gbit sec^{-1} eye-opening.

2. Device Structure and Fabrication

Figure 1a,b, respectively, shows top views of the demonstrated 7 × 7 dual pad VCSEL array (device A) and the single pad reference sample (device B). Figure 1c shows a conceptual 3D diagram of device A, where Zn-diffusion and the oxide-relief apertures are utilized to ensure quasi-SM operation and relax the RC-limited bandwidth, respectively.[9,17] The diameters of the oxide-relief (W_O: 8 μm) and Zn-diffusion apertures (W_Z: 8 μm), and the Zn-diffusion depth (d_Z: 1.2 μm) and positions of light output perforations, are specified in Figure 1c. Both devices (A and B) share the same W_O, W_Z, and d_Z values; the only difference between them is in the design of the p-type electrodes. As shown in Figure 1a,b, in contrast to device B, which has a fully covered p-metal pad for uniform current injection into each aperture, device A has an interdigitated p-type electrode. In this layout, one side of the electrode connects to the RF pad and the other side connects to the DC pad. A certain level of electrical isolation between these two pads can be realized due to the high resistivity of the topmost p-type DBR layers. The special dual pad design used in our array makes nonuniform current injection across different light emission apertures possible, enhancing mutual coupling between neighboring apertures, and leading to a significant improvement in the static and dynamic performance of our array.[18] During high-speed operation, one of the dual pads of device A is for the DC current and the other one is for DC + RF signal injection. The traditional VCSEL array usually has an independent mesa which is etched down to the n-DBR, paralleled by a common electrode on the top side of the array. However, with this type of design, the strong index contrast between the active mesa and the air, which causes a significant loss of evanescent waves, makes optical phase coupling between adjacent VCSEL units difficult. One of the most effective approaches to improve the phase coupling and coherence between neighboring emitters is to use an optical waveguide between the various active mesas.[19,20] Furthermore, for high-brightness performance, it is necessary to downscale the total active area to obtain a dense arrangement of light emission apertures in the array. We thus set the length of the connecting waveguide to be as short as possible. Having a pitch size of 20 μm leads to a small light emission active area of 120 × 120 μm^2 in our 7 × 7 array, as specified in Figure 1a. Compared with previous work,[18] by appropriately increasing the number of light emission apertures from 2 × 2 to 7 × 7, we obtain a larger output power, narrower angle of divergence in the FFPs, and higher brightness, while keeping the same maximum modulation speed at 32 Gbit sec^{-1}. Here, the 20 μm pitch size is limited by device processing capability, although this number may be too large to allow the phenomenon of strong cavity coupling. For this demonstrated array structure, there is evidence of coherence as a superstructure in the FFPs with pitch sizes of ≈12 μm or below.[21,22] In addition, although the mesa shape is not symmetrically circular, a nearly circular (diamond-shaped) wet oxidation aperture can still be obtained, as shown in the inset to Figure 1c. The VCSEL epilayer structure is grown on a $n+$ GaAs substrate, which is composed of four $In_{0.07}Ga_{0.9}As/Al_{0.3}Ga_{0.7}As$ (40/45 Å) MQWs sandwiched between 39-paired n-type and 24-paired p-type $Al_{0.93}Ga_{0.07}As/Al_{0.15}Ga_{0.85}As$ DBR layers with an $Al_{0.98}Ga_{0.02}As$ layer (25 nm thick) above the MQWs for oxidation.[23] Fabry–Perot (FP) dip mapping of the whole VCSEL wafer shows that the cavity resonance wavelength is located at around 850 nm with detuning between the gain peak (838 nm) and FP dip (850 nm) wavelengths at around 12 nm. Such detuning

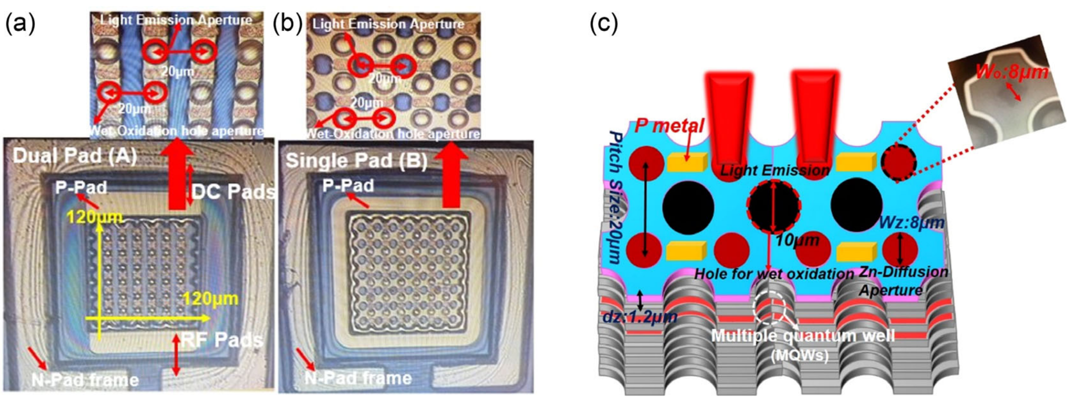

Figure 1. Top view of the demonstrated 7 × 7 VCSEL array for a) device A and b) device B. c) Conceptual cross-section 3D view of active light emission apertures in both devices. An infrared photo of the aperture during the wet oxidation process is shown in the inset.

results in a significant improvement in the 3-dB O–E bandwidth of the VCSEL due to the device self-heating induced red-shift of the gain peak at high-bias currents and high junction temperatures.[24]

3. Measurement Results

The free-space light output power versus current (*L*–*I*) characteristics of devices A and B and a comparison between their current (*I*)–voltage (*I*–*V*) curves are shown in **Figure 2**a–c. In this case, a large area ($1 \times 1\,\text{cm}^2$) power sensor head is used to collect all of the output light from the 49 light emission apertures in our array. The two *I*–*V* curves for device A, shown in Figure 2c, are measured separately from the DC and RF pads for a 7×7 VCSEL array. As can be seen, there is a minor difference in the *I*–*V* curves measured from the DC and RF pads for device A. This slight difference is because the N-contact frame is not perfectly symmetric. As shown in Figure 1a, there is a discontinuity in the N-contact frame on the RF pad side, which leads to a smaller n-contact area and the larger differential resistance measured at this side. Such a gap in the n-contact frame can be beneficial to the yield of the metal lift-off process. Moreover, it should be noted that the differential resistances of device A are significantly greater than that of device B. This is due to the fact that, in device A, the dual electrodes only partially cover the light emission aperture. In contrast, in device B, the *p*-metal area outside of the light emission aperture is fully covered, as shown in Figure 1a,b. For *L*–*I* curve measurement of device A, the injected DC bias current was swept, as shown on the *x*-axis in Figure 2a, onto the RF electrode, and then various DC bias currents, corresponding to the various *L*–*I* traces in this figure, were applied to the DC electrode. It is evident that there is a gradual increase in the total output power from the array following an increase in the bias current on the two isolated electrodes, as expected. Comparison with device B shows that, although device A has a smaller maximum output power (145 vs 170 mW), there is still a slight improvement in the output power (105 vs 94 mW) under the moderate total bias current (180 mA). This can be attributed to the dual-electrode design which facilitates current injection, and effectively minimize current crowding, thereby improving injection efficiency in our 7×7 array. Here, the two major factors limiting the maximum output power (P_{max}) of both devices are the spatial hole burning (SHB) effect, which usually happens in single-mode (SM) VCSELs with perfect Gaussian-like FFPs,[13,14,25] and the thermal effect. The smaller P_{max} of device A than that of B can be attributed to the larger differential resistance of device A, as shown in Figure 2c, which leads to more serious device heating and less P_{max} under high-bias current operation.

To narrow the divergence angles in the FFPs, it is highly desirable for the demonstrated VCSEL to have (quasi-) SM output. **Figure 3**a–c shows the measured bias-dependent output optical spectra of device A obtained using three different injected bias current combinations through the dual electrodes. Figure 3d shows similar measurements but for device B. Here, three different bias currents of 30, 50, and 80 mA were injected onto the DC electrode of device A, while a sweeping bias current was injected into the RF electrodes. The optical spectrum analyzer (ANDO AQ6315A) used had a maximum resolution of around 0.05 nm. The QSM output performance of both devices (A and B) is very similar, thanks to the Zn-diffusion process, which can stabilize the output optical spectra, regardless of the change in bias current combinations. QSM output could be sustained from a low to a high total bias current (≈250 mA). **Figure 4**a–d shows the corresponding bias-dependent 1D and 2D FFPs of device A and device B, respectively, obtained with the three different combinations of bias current. Here, the bias current applied to the DC pad of device A was fixed at 30, 50, or 80 mA, while the current injected onto the RF pad was swept; their values are specified in the figures. As can be seen, both devices could maintain Gaussian FFPs even when the bias current exceeded the saturation output (>250 mA). Moreover, in contrast to device B, device A has a narrower far-field divergence angle (FWHM: ≈8° vs 10° at 250 mA). This can be attributed to the nonuniform current injection from the dual pad which enhances the optical coupling between adjacent VCSEL elements, effectively broadening the near-field distribution,[18,19] which in turn leads to the narrowing of the FFP. **Figure 5** shows the near-field patterns (NFPs) for devices A and B measured under different total bias currents in different combinations, as specified in the figure. It can be clearly seen that, for device A, our dual-electrode design with nonuniform current injection provides weak optical coupling between adjacent

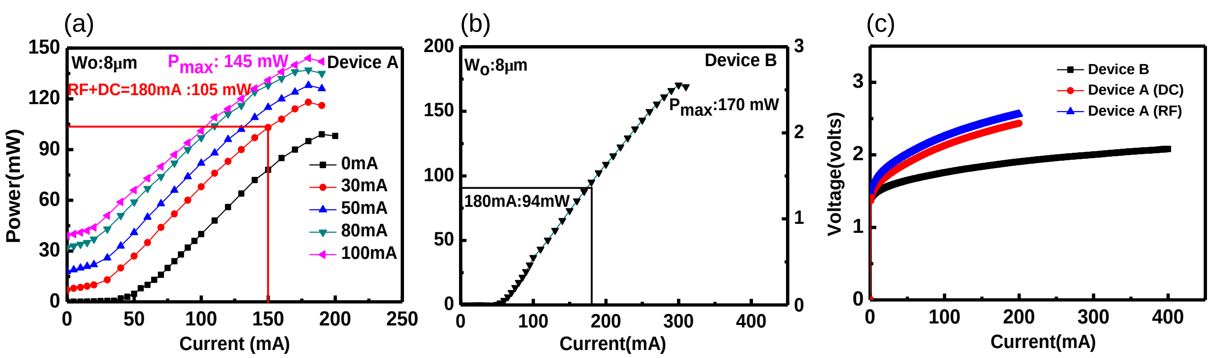

Figure 2. Measured *L*–*I* curves of a) device A and b) device B. c) Measured *I*–*V* curves of device A through the DC and RF pads and for device B ($W_z/W_o/d = 8/8/1.2\,\mu\text{m}$).

ADVANCED PHOTONICS RESEARCH
www.adpr-journal.com

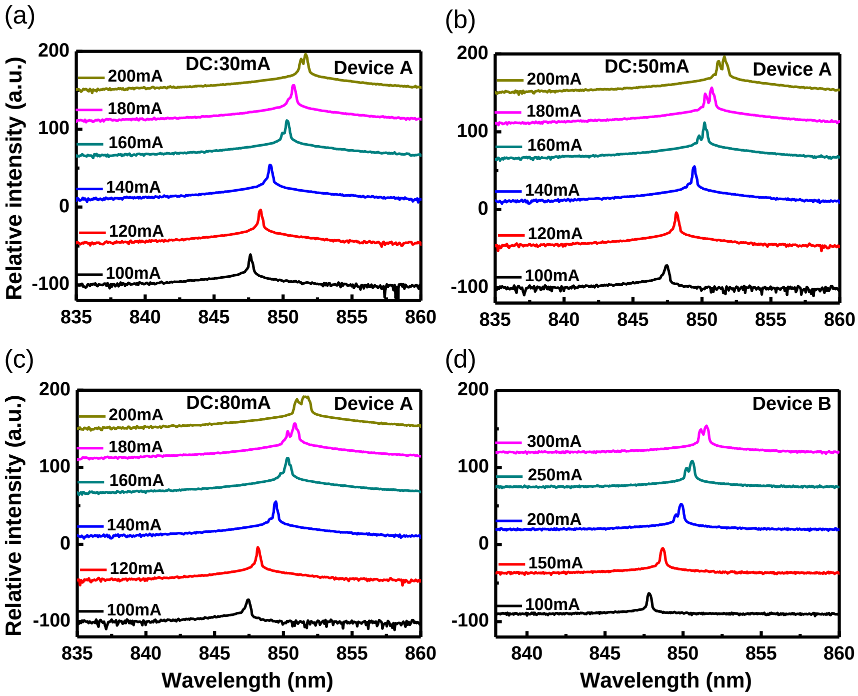

Figure 3. Measured output optical spectra under different bias currents for a) device A (dc electrode: 30 mA), b) device A (dc electrode: 50 mA), c) device A (dc electrode: 80 mA), and d) device B ($W_z/W_o/d = 8/8/1.2\,\mu m$).

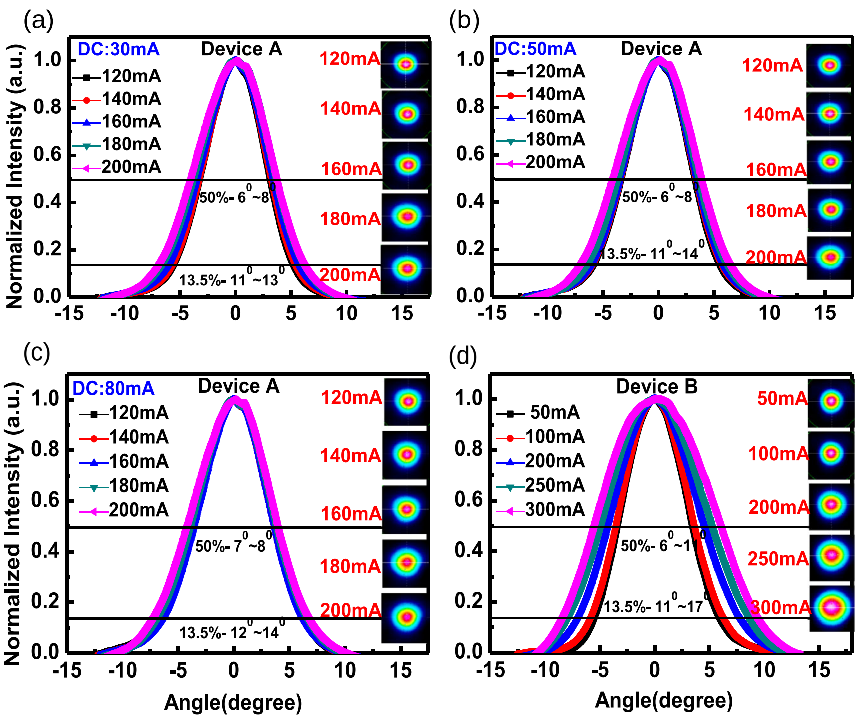

Figure 4. Measured 1D and 2D far-field patterns under different bias currents for a) device A (dc electrode: 30 mA), b) device A (dc electrode: 50 mA), c) device A (dc electrode: 80 mA), and d) device B ($W_z/W_o/d = 8/8/1.2\,\mu m$).

VCSEL units, leading to a significant improvement in its dynamic performance; this will be discussed in greater detail later. In addition, in both devices (A and B), the distribution of NFP in each light emission aperture is highly nonuniform. This can be attributed to the fact that the oxide aperture is diamond-shaped instead of a being perfectly circular, as shown

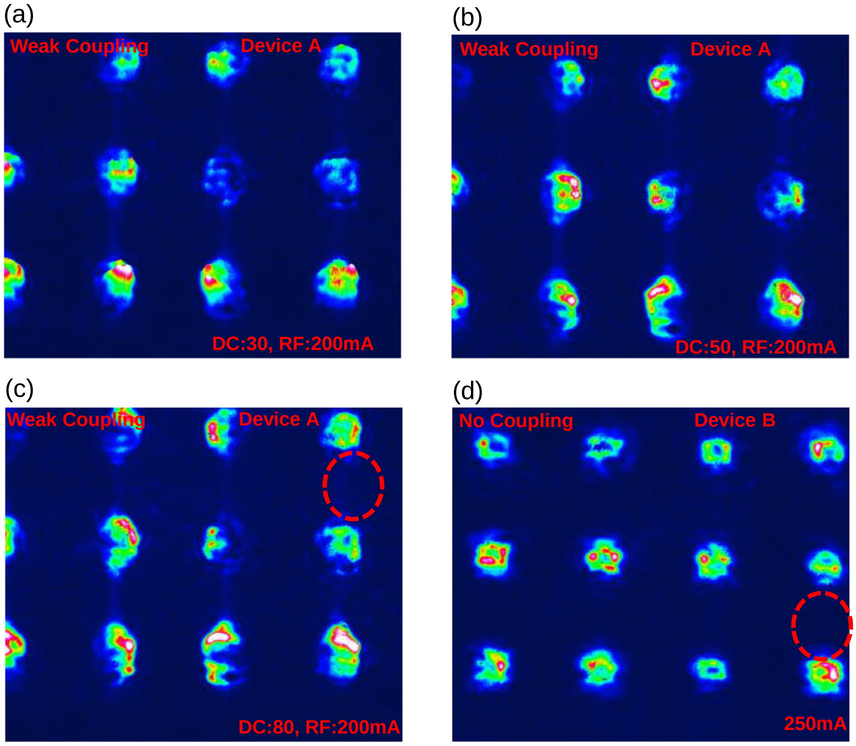

Figure 5. Measured 2D near-field patterns under different bias currents for a) device A (dc electrode: 30 mA), b) device A (dc electrode: 50 mA), c) device A (dc electrode: 80 mA), and d) device B ($W_z/W_o/d = 8/8/1.2$ μm).

in Figure 1c, which leads to the phenomenon of current (gain) crowding in the sharp tips of each aperture and results in the observed nonuniform NFPs.

The high-speed E–O performance of the fabricated devices was measured by a light wave component analyzer (LCA), which was composed of a network analyzer (Anritsu 37397C) and a calibrated photoreceiver module (VI Systems: D50-850 M). **Figure 6**a–c shows the bias-dependent E–O frequency response of device A measured with three different fixed bias currents applied to the DC pads, of 30, 50, and 80 mA, respectively. A comparison of these E–O frequency response traces shows that the one corresponding to the application of a 50 mA bias current onto DC electrode shows the heaviest dampening and widest 3-dB E–O bandwidth. This results in better eye pattern quality, which will be discussed in greater detail later.

Figure 6d shows the measurement results for reference device B obtained under the full range of bias currents. As can be seen, regardless of the bias current combination, device A has a wider 3-dB bandwidth than that does device B (17 vs 13 GHz) under the same total bias current, and the low-frequency roll-off observed with device B has been eliminated. The remarkable dynamic performance of device A is due to the broadening of the near-field patterns originating from the nonuniform current injection from the dual-pad, as shown in Figure 5. This effectively dilutes the cavity photon density and minimizes the SHB effect.[25,26] Moreover, in contrast to the results reported for devices with strongly coupled VCSEL cavities[27–29] which usually have significant bandwidth enhancement induced by strong resonance in their electrical-to-optical (E–O) frequency response, the weak coupling in our array leads to greater dampening of the electrical–optical (E–O) frequency response, a larger 3-dB E–O bandwidth (17 vs 13 GHz), and much better quality of eye-opening than that of the reference device. **Figure 7**a,b shows the back-to-back (BTB) 25 and 32 Gbit sec^{-1} transmission results for device A. During the transmission experiment, a high-speed photoreceiver module (RXM25DF; Thorlabs, Inc), comprised of a GaAs based p–i–n photodiode and a linear amplifier with a 25 GHz 3-dB optical-to-electrical bandwidth for the whole module, was used. A 32 or 25 Gbit s^{-1} non-return-to-zero (NRZ) electrical signal with a pseudo-random binary sequence (PRBS) length of $2^{15}-1$ was generated through a pattern generator. The quality of the eye patterns of all tested devices was evaluated under optimized peak-to-peak driving voltages (V_{pp}) and bias currents. The optimized V_{pp} values of devices A and B are very close, ranging from 0.7 to 1 V. The close values of V_{pp} are mainly due to the quite similar frequency responses of the microwave reflection coefficients (S_{11}) during E–O response measurement (S_{21}) exhibited by these two devices. Figure 7a,b shows clear eye-opening at 25 and 32 Gbit sec^{-1}, respectively, for device A. The values of the timing jitter in each eye pattern, which has clear eye-opening performance, are specified. The superior large-signal transmission performance of device A corresponds to the truth that it has a flatter E–O response, which implies a lower level of RIN noise spectrum,[11] as indicated in Figure 6a, under various current combinations. In contrast, as shown in Figure 7c, the eye pattern diagrams for device B lack

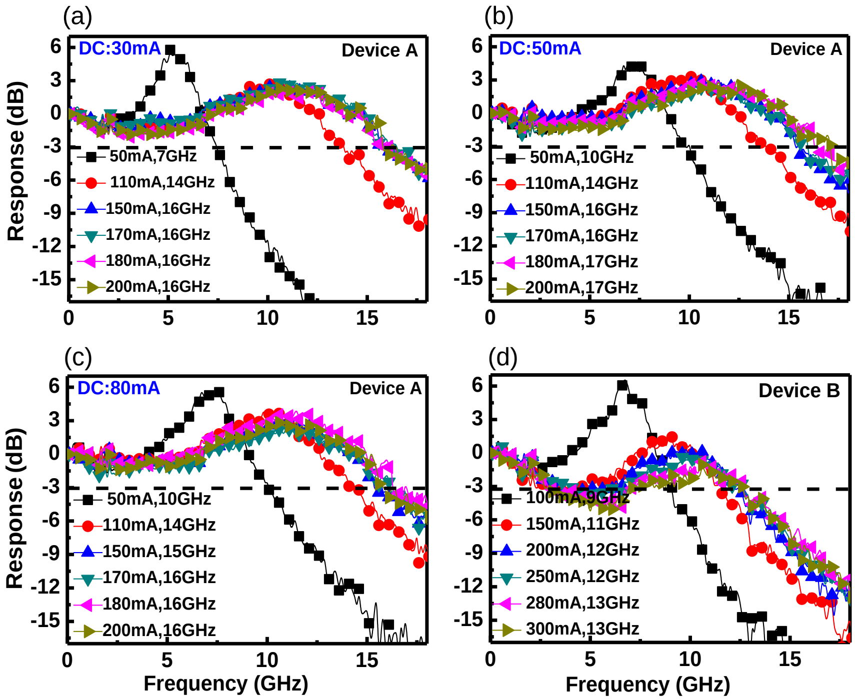

Figure 6. Measured bias-dependent E–O frequency responses of a) device A (dc electrode: 30 mA), b) device A (dc electrode: 50 mA), c) device A (dc electrode: 80 mA), and d) device B ($W_z/W_o/d = 8/8/1.2$ μm).

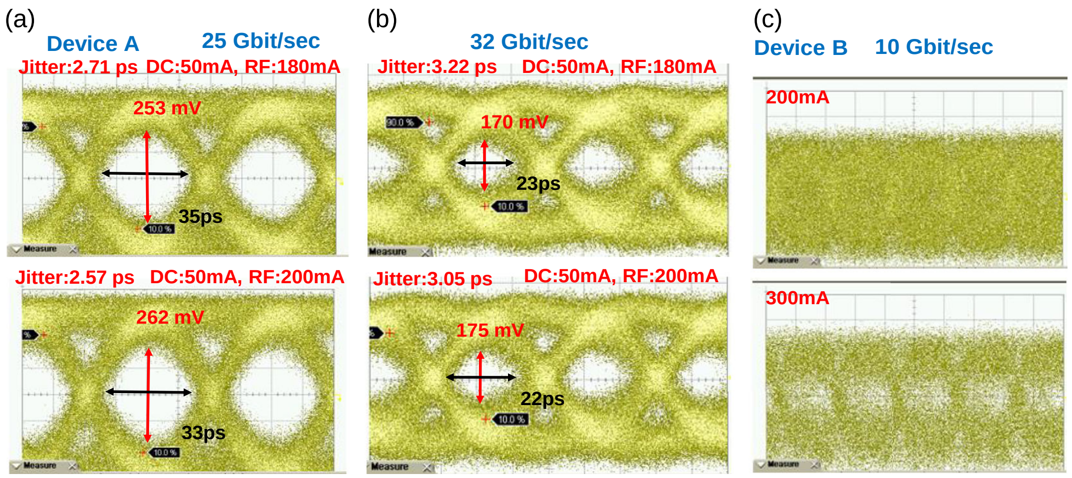

Figure 7. Measured bias-dependent eye patterns of device A at a) 25 Gbit sec^{-1} and b) 32 Gbit sec^{-1}. c) Measured bias-dependent eye patterns of device B at 10 Gbit sec^{-1}. ($W_z/W_o/d = 8/8/1.2$ μm).

clear opening when the data rate is decreased to 10 Gbit sec^{-1}. This result is due to the severe low-frequency roll-off in the E–O frequency response, as shown in Figure 6d.

The superior large-signal transmission performance of device A corresponds to the truth that it has a flatter E–O response, which implies a lower level of RIN noise spectrum,[11] as shown in Figure 6a. Overall, the novel pad layout in our miniaturized array structure demonstrates superior static and dynamic performance when compared to that of its traditional counterpart. **Table 1** gives the benchmark results from recent works on medium-scale VCSEL arrays.[6,16,30–33] The results include the maximum output power, active area, brightness, divergence angles, and speed. The performance of a single VCSEL unit with state-of-the-art brightness performance is also given in this table for comparison.[6] Here, we assume a cone-shaped far-field distribution with point angles of 8° and 11° for devices A and B, respectively, in the calculation of the corresponding steradian and the brightness of the output beam. As can be seen, compared with a single device, there is a significant trade-off between the brightness and the maximum output power due to the increase in the light-emission active area. To overcome this problem, a perfect in-phase mode between each VCESL unit is

Table 1. Benchmark of reported medium-scale VCSEL array.

		Array no.	Aperture [μm]	Active area [μm^2]	Brightness [$kW\,cm^{-2}\,sr^{-1}$]	P_{max} [mW]	Bandwidth [GHz]	Max data rate [Gbps]	Divergence angle [FWHM°]
SD	NCU[6]	–	6	28.7	2900	10 (CW)	16	25	7
SD	Princeton Optronics[31]	–	30	706	30	30 (CW)	–	–	–
Array	NCU[6]	49	7	136 900	5.74	120 (CW)	14	12.5	8
Array	TUB[16]	19	4	49 142	2.06	140 (CW)	17	25	24
Array	NCU (This work) Device B	49	7	14 400	40.8	170 (CW)	13	–	11
Array	NCU (This work) Device A	49	7	14 400	65.95	145 (CW)	17	32	8
Array	Univ. of Wisconsin Madison[31,34]	100	6	8 100	28.2	23 (PW)	–	–	6.5
Array	Univ. of Illinois[32,33]	4	6.5	900	53.1	1.4 (CW)	–	–	3.5

necessary,[32–34] which would result in the narrowing of the divergence angle of the FFP with the increase of device active area, as discussed for the antiguide VCSEL array[31,34] with near-diffraction limited output main beam. Nevertheless, the large internal loss in these antiguide structures and significant side lobes in FFP, which significantly broaden the divergence angle under high-bias current, must be further minimized for CW, high-speed, and high-brightness operation.

4. Conclusion

In this study, we demonstrate a novel design for the electrodes in a high-brightness VCSEL array with a miniaturized light emission active area. The results show that the high-speed data transmission performance can be significantly improved by dividing the electrodes in a compact 7×7 VCSEL array into two parts, one for pure dc current injection and the other for large RF signal modulation. Compared with the single electrode reference array, the demonstrated array with its dual electrodes (dc + RF) design exhibits a greater dampened E–O frequency response and a larger 3-dB E–O bandwidth (17 vs 13 GHz) under the same total bias current (250 mA). These advantages lead to a much better quality of 32 Gbit/sec eye-opening than that of the reference device. In addition, this design can minimize the SHB effect while simultaneously exhibiting a high output power (145 mW), QSM optical spectra at all bias current combinations, and sustained Gaussian-like optical far-field patterns with a narrow divergence angle (FWHM: 8° at 250 mA) and high-brightness output (65.95 $kW\,cm^{-2}\,sr^{-1}$) with the same high output power (≈145 mW). Our dual electrode VCSEL array's superior dynamic and static performance can be attributed to the weak optical coupling between neighboring VCSELs caused by nonuniform current injection through the dual electrodes. Such a novel array design has the potential to further improve the transmission performance of the next generation of OWC channels.

Acknowledgements

This research was funded by the Ministry of Science and Technology in Taiwan under grant number 110-2622-E-008-016. The authors would also like to thank the Intelli-EPI company for their assistance with epitaxial layer growth.

Conflict of Interest

The authors declare no conflict of interest.

Data Availability Statement

The data that support the findings of this study are available from the corresponding author upon reasonable request.

Keywords

fiber optics, optical communications, semiconductor lasers, vertical-cavity surface-emitting lasers

Received: February 28, 2023
Revised: June 5, 2023
Published online:

[1] M. E. Warren, D. Podva, P. Dacha, M. K. Block, C. J. Helms, J. Maynard, R. F. Carson, *Proc. SPIE* **2018**, *10552*, 105520E.
[2] A. M. A. Hassan, X. Gu, M. Nakahama, S. Shinada, M. Ahmed, F. Koyama, *Appl. Phys. Express* **2021**, *14*, 092006.
[3] L. Chorchos, L. Szostkiewicz, N. Ledentsov, G. Bottger, N. Ledentsov, J. P. Turkiewicz, *Opt. Laser Technol.* **2023**, *162*, 109249.
[4] P. Shubert, A. Cline, J. McNally, R. Pierson, *Proc. SPIE* **2017**, *10096*, 100960U.
[5] R. Morgan, Nanosatellite Lasercom System, https://digitalcommons.usu.edu/smallsat/2017/all2017/122/ (accessed: February 2023).
[6] Z. Khan, Y.-H. Chang, T.-L. Pan, Y.-C. Zhao, Y.-Y. Huang, C.-H. Lee, J.-S. Chang, C.-Y. Liu, C.-Y. Lee, C.-Y. Fang, J.-W. Shi, *IEEE Access* **2021**, *10*, 2303.
[7] E. Yagyu, nature.com, https://www.nature.com/articles/d42473-022-00105-1 (accessed: September 2022).
[8] M. Yoshida, M. De Zoysa, K. Ishizaki, Y. Tanaka, M. Kawasaki, R. Hatsuda, B. Song, J. Gelleta, S. Noda, *Nat. Mater.* **2019**, *18*, 121.
[9] Z. Khan, J.-C. Shih, R.-L. Chao, T.-L. Tsai, H.-C. Wang, G.-W. Fan, Y.-C. Lin, J.-W. Shi, *Optica* **2020**, *7*, 267.
[10] J.-L. Yen, K.-L. Chi, J.-W. Jiang, Y.-J. Yang, J.-W. Shi, *IEEE J. Quantum Electron.* **2014**, *50*, 787.

[11] D. M. Kuchta, J. Gamelin, J. D. Walker, J. Lin, K. Y. Lau, J. S. Smith, *Appl. Phys. Lett.* **1993**, *62*, 1194.
[12] P. Westbergh, J. S. Gustavsson, B. Kögel, A. Haglund, A. Larsson, *IEEE J. Sel. Top. Quantum Electron.* **2011**, *17*, 1603.
[13] A. Haglund, J. S. Gustavsson, P. Modh, A. Larsson, *IEEE Photonics Technol. Lett.* **2005**, *17*, 1602.
[14] J.-W. Shi, Z.-R. Wei, K.-L. Chi, J.-W. Jiang, J.-M. Wun, I.-C. Lu, J. Chen, Y.-J. Yang, *IEEE/OSA J. Lightwave Technol.* **2013**, *31*, 4037.
[15] P. Moser, M. Zorn, J. A. Lott, *J. Phys.: Photonics* **2020**, *2*, 04LT01.
[16] N. Haghighi, W. Głowadzka, T. Czyszanowski, M. Zorn, J. A. Lott, in *2022 IEEE Photonics Conf. (IPC)*, Vancouver, BC, Canada **2022**, https://doi.org/10.1109/IPC53466.2022.9975628.
[17] C.-L. Cheng, N. Ledentsov, Z. Khan, J.-L. Yen, N. N. Ledentsov, J.-W. Shi, *IEEE J. Sel. Top. Quantum Electron.* **2019**, *25*, 1700507.
[18] Y.-C. Zhao, Z. Ahmad, W.-M. Long, Z. Khan, N. Ledentsov, M.-B. Sanayeh, T.-L. Pan, C.-C. Chen, C.-J. Chang, T.-C. Lu, N. N. Ledenstov, J.-W. Shi, *Opt. Express* **2022**, *30*, 26690.
[19] J.-C. Shih, Z. Khan, Y.-H. Chang, J.-W. Shi, *IEEE J. Sel. Top. Quantum Electron.* **2022**, *28*, 1501211.
[20] F. Koyama, X. Gu, *IEEE J. Sel. Top. Quantum Electron.* **2013**, *19*, 1701510.
[21] E. Lamothe, L.-D. A. Lundeberg, E. Kapon, *Opt. Lett.* **2011**, *36*, 2916.
[22] N. Ledentsov, L. Chorchos, O. Y. Makarov, M. B. Sanayeh, J.-R. Kropp, I. E. Titkov, V. A. Shchukin, V. P. Kalosha, J. P. Turkiewicz, N. N. Ledentsov, *Proc. SPIE* **2022**, *12020*, 1202008.
[23] Intelligent Epitaxy Technology, Inc., Richardson, TX, http://intelliepi.com.
[24] H. Li, P. Wolf, P. Moser, G. Larisch, A. Mutig, J. A. Lott, D. H. Bimberg, *IEEE J. Quantum Electron* **2014**, *50*, 613.
[25] T. Gründl, P. Debernardi, M. Muller, C. Grasse, P. Ebert, K. Geiger, M. Ortsiefer, G. Bohm, R. Meyer, M. C. Amann, *IEEE J. Sel. Top. Quantum Electron.* **2013**, *19*, 1700913.
[26] Y. Liu, W. C. Ng, B. Klein, K. Hess, *IEEE J. Quantum Electron.* **2003**, *39*, 99.
[27] S. T. M. Fryslie, M. P. T. Siriani, D. F. Siriani, M. T. Johnson, K. D. Choquette, *IEEE Photonics Technol. Lett.* **2015**, *27*, 415.
[28] X. Gu, M. Nakahama, A. Matsutani, M. Ahmed, A. Bakry, F. Koyama, *Appl. Phys. Express* **2015**, *8*, 082702.
[29] E. Heidari, H. Dalir, M. Ahmed, V.-J. Sorger, R.-T. Chen, *Nanophotonics* **2020**, *9*, 4743.
[30] J.-F. Seurin, G. Xu, Q. Wang, B. Guo, R. V. Leeuwen, A. Miglo, P. Pradhan, J. D. Wynn, V. Khalfin, C. Ghosh, *Proc. SPIE* **2010**, *7615*, 76150F.
[31] D. Zhou, A. P. Napartovich, N. N. Elkin, D. V. Vysotsky, L. J. Mawst, *Proc. SPIE* **2002**, *4649*, https://doi.org/10.1117/12.469231.
[32] D. F. Siriani, K. D. Choquette, *Electron. Lett.* **2010**, *46*, 712.
[33] D. F. Siriani, K. D. Choquette, *IEEE Photonics Technol. Lett.* **2011**, *23*, 167.
[34] L. Bao, N.-H. Kim, L. J. Mawst, N. N. Elkin, V. N. Troshchieva, D. V. Vysotsky, A. P. Napartovich, *Appl. Phys. Lett.* **2004**, *84*, 320.

